

Freqformer: Frequency-Domain Transformer for 3-D Visualization and Quantification of Human Retinal Circulation

Lingyun Wang, Bingjie Wang, Jay Chhablani, Jose Alain Sahel, and Shaohua Pi

Abstract—We introduce Freqformer, a novel Transformer-based architecture designed for 3-D, high-definition visualization of human retinal circulation from a single scan in commercial optical coherence tomography angiography (OCTA). Freqformer addresses the challenge of limited signal-to-noise ratio in OCTA volume by utilizing a complex-valued frequency-domain module (CFDM) and a simplified multi-head attention (Sim-MHA) mechanism. Using merged volumes as ground truth, Freqformer enables accurate reconstruction of retinal vasculature across the depth planes, allowing for 3-D quantification of capillary segments (count, density, and length). Our method outperforms state-of-the-art convolutional neural networks (CNNs) and several Transformer-based models, with superior performance in peak signal-to-noise ratio (PSNR), structural similarity index measure (SSIM), and learned perceptual image patch similarity (LPIPS). Furthermore, Freqformer demonstrates excellent generalizability across lower scanning density, effectively enhancing OCTA scans with larger fields of view (from 3×3 mm² to 6×6 mm² and 12×12 mm²). These results suggest that Freqformer can significantly improve the understanding and characterization of retinal circulation, offering potential clinical applications in diagnosing and managing retinal vascular diseases.

Index Terms—Retinal circulation, Optical coherence tomography angiography (OCTA), Transformer, 3-D visualization, Frequency-domain enhancement.

I. INTRODUCTION

RETINAL blood vessels, carrying nutrients and oxygen to supply retinal cells, are essential for maintaining tissue homeostasis and visual function [1], and of vital importance in characterizing retinal vascular diseases. Recently, as a functional extension of optical coherence tomography (OCT), OCT angiography (OCTA) is emerging to resolve retinal microvasculature *in vivo* by detecting the moving contrast of blood flow [2]. Although OCTA can provide 3-D visualization

of retinal circulation, current analysis primarily relies on 2-D OCTA *en face* images projected from specific slabs. The *en face* approach may oversimplify the inherently 3-D nature of the OCTA volume, limiting its potential to fully elucidate the complex architecture of the retinal microvascular network, constraining the inherent 3-D nature of OCTA volume and diminishing its significance in understanding 3-D retinal microvascular network. A critical technical challenge in performing direct 3-D analysis of OCTA volumes arises from their limited quality, characterized by a low signal-to-noise ratio (SNR) and poor vascular connectivity across individual depth planes. As a result, the retinal circulation remains incompletely understood, particularly in terms of its 3-D organization and intricate relationship with the retinal layers [3], [4].

Shape-based filtering (such as Hessian filtering [5]), has been widely used to enhance OCTA volume. It works by identifying and enhancing the tubular structures corresponding to blood vessels. However, it is highly sensitive to noise due to the second-order derivatives [6] and frequently causes ghost blood vessels. Other conventional algorithms, such as wavelet transform [7] and compressive sensing [8], also face challenges in achieving an optimal balance between noise reduction and vessel enhancement. Recently, deep learning has emerged as a promising approach for enhancing retinal circulations [9]. These methods can be broadly categorized into two avenues: 1) Super-resolution-based approach. In this method, networks are trained using paired low-resolution (such as 6×6 mm²) and high-resolution (3×3 mm²) angiograms to enhance the OCTA images [10], [11]. 2) Frame-averaging-based approach. Here, the network takes a single scan image as input and uses a merged image as ground truth to enhance the angiograms [12]. However, these methods are limited to 2-D *en face* projection images due to the low quality of individual depth plane images in OCTA, making the training process highly challenging. To the best of our knowledge, the only reported approach for obtaining high-definition 3-D vasculature from a single OCTA scan involves training a network to segment blood vessels [13], [14], which is a simplified task for enhancing the angiograms. However, the manual annotation of numerous depth plane images required by this method is highly time-consuming and poses significant challenges for annotators in accurately labeling capillaries. Moreover, the lack of angiogram decorrelation information in segmentation limits its utility [15].

In this work, we introduce Freqformer, a frequency-domain Transformer-based architecture designed to reconstruct the 3-D organization of retinal circulation from a single commercial

This work was supported in part by Eye & Ear Foundation of Pittsburgh, NIH CORE Grant P30 EY08098 and an unrestricted grant from Research to Prevent Blindness to the Department of Ophthalmology, as well as the University of Pittsburgh Center for Research Computing through the resources provided. Specifically, this work used the H2P cluster, which is supported by NSF award number OAC-2117681. (*Corresponding author: Shaohua Pi.*)

Lingyun Wang and Shaohua Pi are with the Department of Ophthalmology, University of Pittsburgh, Pittsburgh, PA 15213, USA, and also with the Department of Bioengineering, University of Pittsburgh, Pittsburgh, PA 15261, USA (e-mail: LingyunWang@pitt.edu; shaohua@pitt.edu).

Bingjie Wang, Jay Chhablani, and Jose Alain Sahel are with the Department of Ophthalmology, University of Pittsburgh, Pittsburgh, PA 15213, USA (e-mail: biw35@pitt.edu; chhablanijk2@upmc.edu; sahelja@upmc.edu).

This work has been submitted to the IEEE for possible publication. Copyright may be transferred without notice, after which this version may no longer be accessible.

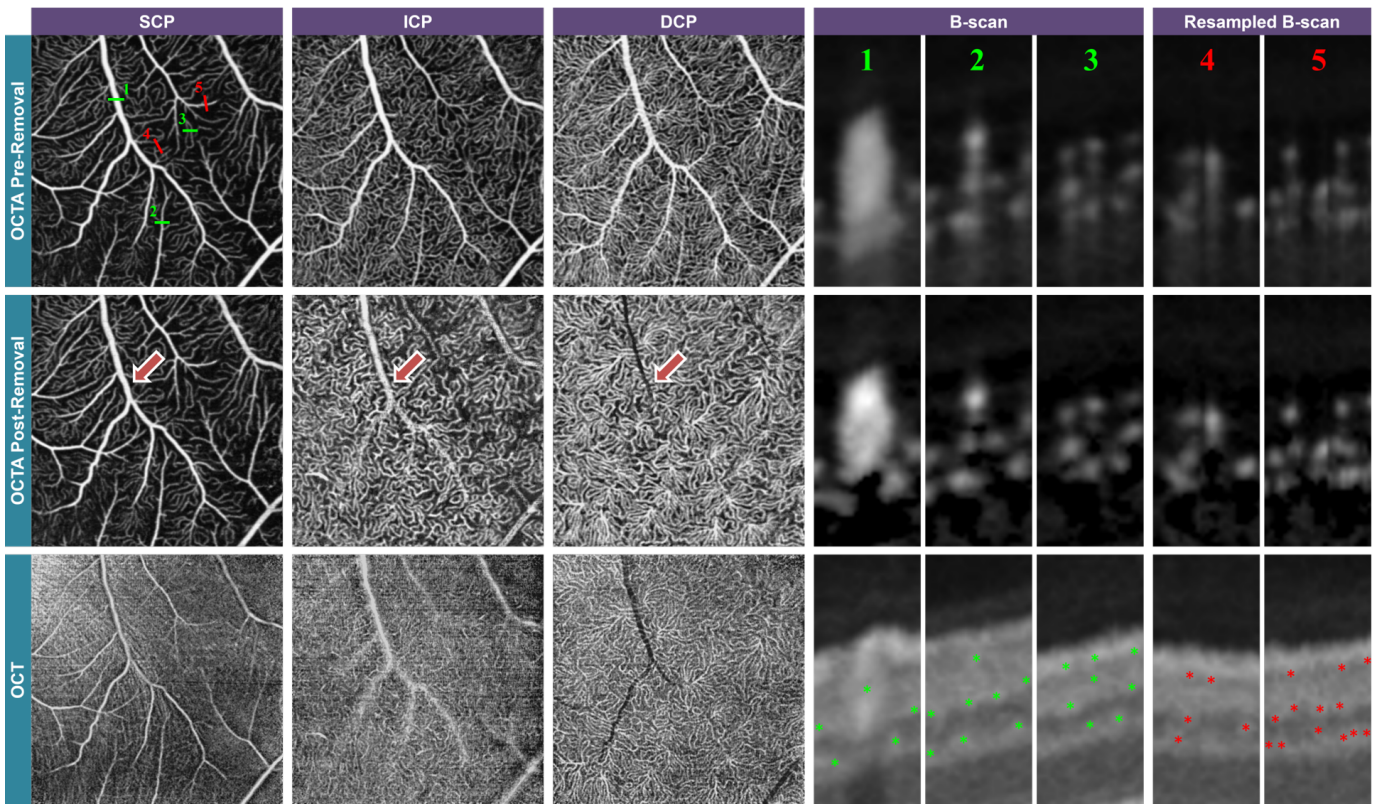


Fig. 1. Tail artifact removal of human retinal circulation in OCTA, using OCT images as reference to confirm the true axial position of vessel caliber. The location of the B-scan and the resampled B-scan, as well as their blood vessels were marked by the green line and the red line, respectively, highlighting the tail artifacts removal performance in large blood vessel (1, $d \sim 100\mu\text{m}$), middle blood vessel (2, $d \sim 30\mu\text{m}$), and capillaries (3, 4, 5, $d \sim 10\mu\text{m}$). The tail artifact of the blood vessel (denoted by a red arrow) was removed in the deep capillary plexus. SCP, superficial capillary plexus. ICP, intermediate capillary plexus. DCP, deep capillary plexus.

OCTA scan. It takes advantage of Transformer [9], [16]–[18], a revolutionary technique with self-attention mechanism to mitigate the limitation of CNNs (small receptive field struggling to capture global (long-range pixel) interactions). The highlights of Freqformer include:

(1) Complex-Valued Frequency-Domain Module (CFDM) which leverages frequency information to address Transformers’ limitations in extracting high-frequency features, significantly enhancing the resolution and connectivity of OCTA images.

(2) Efficient Transformer layer which integrates Simplified Multi-Head Attention (Sim-MHA) and Depth-Wise Convolution Feed-Forward Network (DFFN) to reduce space complexity through cross-covariance attention mechanism.

(3) Superior performance which outperforms existing CNN-based and Transformer-based methods in visual and quantitative metrics for enhanced retinal circulation imaging.

(4) Exceptional generalizability with robustness in being applied to larger field of view scans ($6 \times 6 \text{ mm}^2$ and $12 \times 12 \text{ mm}^2$), effectively improving low-density scans obtained from commercial devices.

(5) Clinical utility and quantification with preservation of 3-D vascular integrity and analysis of capillary segments, providing valuable insights into retinal vascular health and advancing diagnostic capabilities.

II. METHOD

A. Data Acquisition and Preprocessing

This study involved healthy human subjects recruited from the UPMC Vision Institute, Department of Ophthalmology at the University of Pittsburgh, Pittsburgh, PA USA. The study was conducted following strict ethical guidelines, with all participants signing informed consent forms, in compliance with the Declaration of Helsinki. Ethical approval was obtained from the institutional review boards of the University of Pittsburgh. OCT/A scans were acquired using a PLEX® Elite 9000 swept-source OCT (ZEISS, Dublin, CA). Each imaging session consisted of 400 A-lines per B-scan, and 400 B-scans per volume, with a total of 10 repeated volumes, covering a $3 \times 3 \text{ mm}^2$ field of view across various retinal regions.

To generate ground truth, the 10 repeated volumes of each OCT/A session were registered and merged using recently developed algorithms [19], [20]. Briefly, the 3-D registration algorithm independently aligned the lateral and axial directions, taking advantage of the negligible angle variation of the probing light with the retinal tissue, resulting in nearly invariant A-line profiles across repeats. In the lateral direction, non-rigid registration was performed by aligning retinal vascular patterns in *en face* images. In the axial direction, a depth transformation matrix was computed by calculating the cross-correlation of A-line profiles and identifying the axial shifts

with maximal correlation values. The registered volumes were then averaged to produce high-definition OCT/A volumes as the ground truth for training.

To accurately capture true retinal circulation in 3-D, removing tail artifacts of blood vessels is a critical step [21]. Several algorithms have been developed to address this issue [22]–[24]. However, they were developed to maximize integrity of capillary plexuses in *en face images*, often neglecting the actual caliber of retinal vessels. As a result, they tend to lose penetrating and connecting vessels/capillaries, limiting their utility for appreciating 3-D retinal circulation. To address this challenge, we propose a moving average filter (MAF) method. This method leverages the fact that artifact voxels typically have smaller angiogram values than the real vessel voxels located anteriorly. Specifically, to obtain an artifact-free OCTA volume A_{PR} , we designed a moving filter with a size of $50 \mu\text{m}$ along the axial direction with an empirical residual coefficient of 0.8 (Eq. 1). As demonstrated in Fig. 1, the proposed method effectively removed tail artifacts from the superficial capillary plexus (SCP), preserving the integrity of the intermediate capillary plexus (ICP) and deep capillary plexus (DCP). The caliber of retinal microvasculature in the post-removal OCTA B-scan images resembled that observed in cross-sectional OCT B-scan images, ensuring excellent preservation of penetrating vessels and capillaries. These results underscore the effectiveness of the proposed MAF method for robust and accurate tail artifact removal in 3-D OCTA imaging.

$$A_{PR} = \sqrt{A_n^2 - 0.8 \sum_{i=n-11}^{n-1} A_i^2} \quad (1)$$

B. Freqformer

1) *Overall Architecture*: Freqformer employs a 4-stage symmetric encoder-decoder backbone architecture designed to process single scan OCTA images (Fig. 2). Given an input OCTA image $\mathbf{I} \in \mathbb{R}^{H \times W \times 1}$, Freqformer first applies a 3×3 convolutional layer to extract shallow feature $\mathbf{F}_0 \in \mathbb{R}^{H \times W \times C}$. After that, the encoder-decoder structure was used to extract the deep features with encoders reducing the spatial resolution of the feature map while doubling the number of channels using pixel-unshuffle operation as the stage grows, and decoders performing the opposite operations to restore the original resolution. At stages 1-3, up-sampled feature maps are concatenated with their corresponding encoder output, with channel dimension reduced by half using a 1×1 convolutional layer. These skip connections preserve crucial spatial information and minimize the loss of fine details during the down-sampling and up-sampling processes. Additionally, to improve generalization, a drop path rate of 0.1 is applied, randomly dropping paths during training to regularize the network. After passing through the encoder-decoder, feature maps undergo further refinement, resulting in $\mathbf{I}_r \in \mathbb{R}^{H \times W \times 1}$ after a 3×3 convolutional layer. The enhanced OCTA image is then generated by adding \mathbf{I} to \mathbf{I}_r , effectively merging the original image with the refined deep features to produce a high-quality output.

Each stage of the encoder-decoder architecture and refinement comprises multiple Freqformer blocks. In each block, the feature map $\mathbf{F}_i \in \mathbb{R}^{H \times W \times C}$ is split into two parts $\mathbf{X}_1 \in \mathbb{R}^{H \times W \times \alpha C}$ and $\mathbf{X}_2 \in \mathbb{R}^{H \times W \times (1-\alpha)C}$ along the channel dimension. \mathbf{X}_1 is processed by the Transformer layer, which includes the Simplified Multi-Head Attention (Sim-MHA) and Depth-Wise Convolution Feed-Forward Network (DFFN) for extracting spatial features. \mathbf{X}_2 is processed by the Complex-valued Frequency-Domain Module (CFDM) to capture features in the frequency domains. This dual-branch strategy enables Freqformer to leverage complementary spatial and frequency domain features, ensuring enhanced representation and reconstruction capabilities for OCTA images.

2) *Simplified Multi-Head Attention (Sim-MHA)*: With feature map $\mathbf{X} \in \mathbb{R}^{H \times W \times C}$, conventional multi-head attention (MHA) computes a weighted sum of the values $\hat{\mathbf{V}} \in \mathbb{R}^{h \times HW \times d}$, with attention weights $\mathbf{A} \in \mathbb{R}^{h \times HW \times HW}$ derived from the dot-product of queries $\hat{\mathbf{Q}} \in \mathbb{R}^{h \times HW \times d}$ and transposed keys $\hat{\mathbf{K}}^T \in \mathbb{R}^{h \times d \times HW}$, where d and h denote the number of dimensions and heads, respectively. However, MHA's quadratic space complexity $\mathcal{O}(hH^2W^2)$ pose challenges for OCTA images with large size as it significantly exceeds the linear complexity of CNNs $\mathcal{O}(HWC_{out})$. To address this, we introduce cross-covariance (CC) attention [25], where attention weights $\mathbf{A} \in \mathbb{R}^{h \times C \times C}$ are computed across channels instead of tokens, using the cross-covariance matrix $\hat{\mathbf{K}}^T \hat{\mathbf{Q}}$. This approach reduces space complexity to $\mathcal{O}(C^2/h)$, making it scale linearly with image size.

Specifically, in standard MHA, there are four linear transformations (W_q , W_k , W_v , and $W_{projection}$) applied to compute queries (\mathbf{Q}), keys (\mathbf{K}), values (\mathbf{V}), and output features. However, W_v and $W_{projection}$ are removed because their identity components tend to become dominant as Transformer converges [26], [27]. To improve local context representation, a 3×3 depth-wise convolutional layer (DConv) is integrated after the W_q and W_k linear transformations, implemented via 1×1 convolution. Unlike conventional vanilla convolutional layers, DConv operates channel-wise, rather than across all channels, thereby reducing computational cost to $\sim 1/2C$. The Sim-MHA operation is defined as:

$$\begin{aligned} \mathbf{X}_{\text{Sim-MHA}} &= \hat{\mathbf{X}} \cdot \text{softmax}(\hat{\mathbf{K}}^T \hat{\mathbf{Q}} / \tau), \\ \mathbf{K} &= \text{LN}(\mathbf{X}) W_k W_D, \\ \mathbf{Q} &= \text{LN}(\mathbf{X}) W_q W_D, \end{aligned} \quad (2)$$

where W_D and $\text{LN}(\cdot)$ represent the depth-wise convolution transformation layer and the layer normalization, respectively. τ is a trainable scaling factor to prevent gradients vanishing caused by the softmax function, and $\hat{\mathbf{X}}$, $\hat{\mathbf{K}}$, and $\hat{\mathbf{Q}}$ the reshaped form of \mathbf{X} , \mathbf{K} , and \mathbf{Q} with corresponding dimensions required by the self-attention mechanism [16].

3) *Depth-Wise Convolution Feed-Forward Network (DFFN)*: The feed-forward network (FFN) [16], or multi-layer perceptron, introduces non-linearity to enhance the learning complex patterns in Transformer. In the proposed DFFN, two linear transformations are applied using 1×1 convolutions to expand and reduce channels. A 3×3 DConv layer, similar to that in Sim-MHA, is integrated to enhance

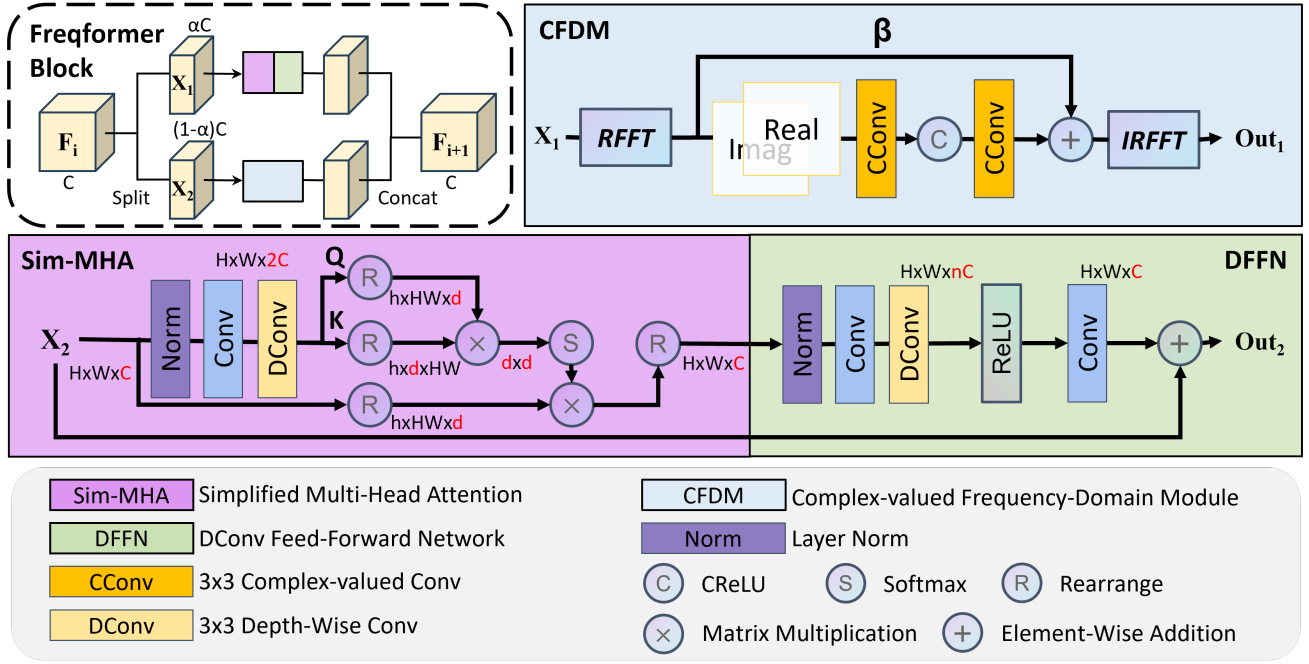


Fig. 2. Framework of proposed Freqformer. RFFT, real-valued fast Fourier transform. IRFFT, Inverse real-valued fast Fourier transform.

local context representation. The skip connection used in conventional MHA is removed, directly connecting the input to the DFFN output. DFFN is defined as:

$$\text{ReLU}((\text{LN}(\mathbf{X}_{\text{Sim-MHA}})W_p^0 + b_p^0)W_D + b_D)W_p^1 + b_p^1 + \mathbf{X}, \quad (3)$$

where b_p^0 , b_p^1 , and b_D are biases of linear transformations W_p^0 and W_p^1 , and the 3×3 DConv layer W_D , respectively.

4) Complex-valued Frequency-Domain Module (CFDM):

As mentioned above, the essence of MHA is a weighted sum of values. This summation process, whether simplified or not, tends to diminish high-frequency features in the Transformer [28]. To address this, we introduce CFDM, which directly learns complex features in the frequency domain [29].

In CFDM, a real-valued fast Fourier transform (RFFT) is applied to the feature map $\mathbf{X} \in \mathbb{R}^{H \times W \times C}$, generating a frequency representation $\mathcal{F}(\mathbf{X}) \in \mathbb{C}^{H \times \lfloor \frac{W}{2} + 1 \rfloor \times C}$, reducing redundancy and computational cost without losing information due to Hermitian symmetry. After the RFFT, two complex-valued convolutional layers (CConv) are employed to process frequency-domain features [30]. For an input $\mathcal{F}(\mathbf{X}) = x + iy$ and a convolution $\mathbf{W} = u + iv$, the operation is $\mathcal{F}(\mathbf{X}) * \mathbf{W} = (x * u - y * v) + i(x * v + y * u)$. Therefore, the gradient of back-propagation can be expressed as:

$$\frac{\partial L(\mathcal{F}(\mathbf{X}) * \mathbf{W})}{\partial \mathbf{W}} = \frac{\partial L(\mathcal{F}(\mathbf{X}) * \mathbf{W})}{\partial \mathcal{F}(\mathbf{X}) * \mathbf{W}} * \mathcal{F}(\mathbf{X}), \quad (4)$$

where $L(\cdot)$ denotes the loss function. The real part of $\frac{\partial L(\mathcal{F}(\mathbf{X}) * \mathbf{W})}{\partial \mathbf{W}}$ is $\Re\left(\frac{\partial L(\mathcal{F}(\mathbf{X}) * \mathbf{W})}{\partial \mathcal{F}(\mathbf{X}) * \mathbf{W}}\right) * x - \Im\left(\frac{\partial L(\mathcal{F}(\mathbf{X}) * \mathbf{W})}{\partial \mathcal{F}(\mathbf{X}) * \mathbf{W}}\right) * y$ while the imaginary part is $\Re\left(\frac{\partial L(\mathcal{F}(\mathbf{X}) * \mathbf{W})}{\partial \mathcal{F}(\mathbf{X}) * \mathbf{W}}\right) * y + \Im\left(\frac{\partial L(\mathcal{F}(\mathbf{X}) * \mathbf{W})}{\partial \mathcal{F}(\mathbf{X}) * \mathbf{W}}\right) * x$. It is worth noting that, although the receptive field of CConv is limited, it still captures global

context as each frequency component represents a global characteristic of the entire image.

Next, CReLU, which performs conventional ReLU on the real part and the imaginary part of feature maps separately, conducts non-linear activation [31]. However, this activation approach can alter the amplitude and phase simultaneously, potentially disrupting the original frequency information. To mitigate this, we introduce a dynamic skip connection between the original complex-valued matrix and the output in the frequency domain, controlled by a trainable parameter β . Finally, inverse RFFT is employed to convert the frequency-domain enhanced feature back to spatial domain.

C. 3-D Analysis of Retinal Circulation

To quantify retinal circulation, enhanced OCTA volumes are binarized using a thresholding approach, where voxels with angiogram values larger than the threshold (50/255) are determined as blood vessels. As described in our previous work [32], the 3-D binary masks are then skeletonized to shrink vascular diameter and highlight connectivity information. Next, the number of neighboring vascular voxels is counted for each voxel in 3-D space to identify bifurcation points, which are characterized by having exactly three neighboring vascular voxels. These bifurcation points are unique among body points of blood vessels with two neighboring vascular voxels and end points with only one neighboring vascular voxel. Therefore, by removing these bifurcation points, vessel segments can be isolated and extracted automatically. It should be noted that small fragments with lengths equal or less than six voxels are considered as noise and excluded from the analysis. Quantitative metrics, including capillary segment count (N), segment density (N/mm^3), segment length (voxel), are calculated all within the inner retina volume.

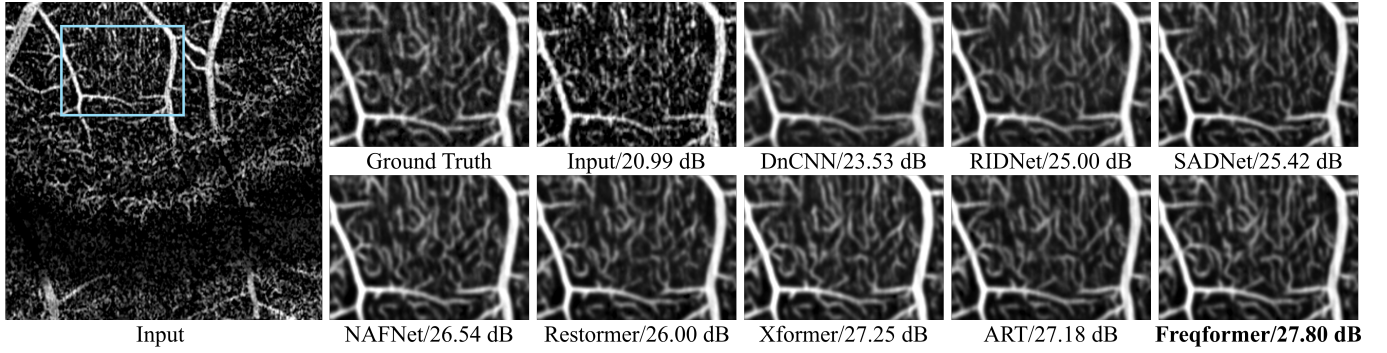


Fig. 3. Comparisons of different deep learning enhancement methods with PSNR values listed.

Statistical comparisons among the three groups (single scan, enhanced scan, and merged scan) are performed using one-way ANOVA followed by Tukey's HSD test. A p-value smaller than 0.05 is considered significant in this study.

III. EXPERIMENTS AND RESULTS

A. Data Preparation and Implementation Details

We randomly selected $N=3,600$ single-merged pairs of depth plane OCTA images ($400 \text{ px} \times 400 \text{ px}$) from 20 scans across 14 subjects. The dataset was divided into 90% for training and 10% for validation. An additional 400 pairs of images from extra scans not included in the training data, were used to evaluate performance.

The number of Freqformer blocks was set to [2, 4, 4, 6, 4, 4, 2] in the stage of encoder-decoder, and to 4 in the refinement module. Following typical settings in other Transformer methods [33], [34], the number of heads in each stage of the encoder-decoder was set to [1, 2, 4, 8, 4, 2, 1], with 1 head used in the refinement module. Additionally, the number of channels was 48 for the feature map input into the encoder-decoder. In the Transformer layer, the Sim-MHA employed bias-free linear transformations, while the DFFN used biased linear transformations, with an expansion factor of 2.66.

The model was trained using AdamW optimizer [35] ($\beta_1 = 0.9$, $\beta_2 = 0.999$, weight decay of $1e^{-4}$) and L_1 loss. The batch size was set to 1, and the model was trained for 480,000 iterations with an initial learning rate $1e^{-4}$, halved every 20 epochs until convergence. The reference networks were trained following their original implementation details. All experiments were implemented in Python 3.8 with Pytorch 2.2.0 deep learning framework on a single NVIDIA A100 GPU.

B. Evaluation Metrics

The performance of Freqformer was assessed using three image quality metrics: peak signal-to-noise ratio (PSNR), structural similarity index measure (SSIM), and learned perceptual image patch similarity (LPIPS), as detailed below:

$$\text{PSNR} = 10 \log_{10} \left(\frac{\max(I)^2}{\frac{1}{N} \sum_{i=1}^N (I(i) - I_{GT}(i))^2} \right), \quad (5)$$

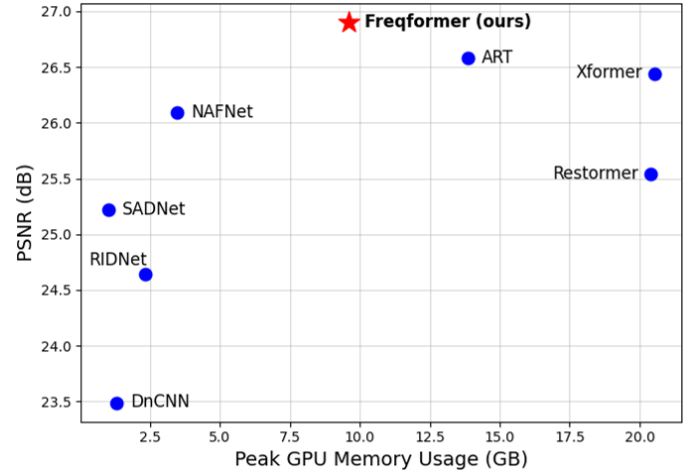


Fig. 4. PSNR vs peak GPU memory usage graph.

$$\text{SSIM} = \frac{(2\mu_I\mu_{I_{GT}} + C_1)(2\sigma_{II_{GT}} + C_2)}{(\mu_I^2 + \mu_{I_{GT}}^2 + C_1)(\sigma_I^2 + \sigma_{I_{GT}}^2 + C_2)}, \quad (6)$$

$$\text{LPIPS} = \sum_l \omega_l \frac{1}{N} \sum_{i=1}^N \|\phi_l(I(i)) - \phi_l(I_{GT}(i))\|_2^2, \quad (7)$$

where I and I_{GT} are the enhanced image and the ground truth. N is the number of pixels in the image. μ and σ denote the mean and standard deviation for an image, while $\sigma_{II_{GT}}$ is the covariance between I and I_{GT} . The constants C_1 and C_2 in SSIM are set to 0.01 and 0.03. ϕ_l and ω_l denote the l -th layer and its weight factor of the pre-trained AlexNet. These metrics were used to comprehensively evaluate image reconstruction quality, focusing on fidelity and perceptual similarity to the ground truth.

C. Performance and Comparison with Other Methods

To evaluate the effectiveness of the proposed Freqformer, we compared it with several state-of-the-art networks, including three transformer-based models and four CNN-based models.

As shown in Fig. 3, the capillaries in the depth plane image from single scan (input) exhibit discontinuity and noise, making it difficult to study the intricate retinal circulation. Due to their limited receptive fields, CNNs primarily focus on local

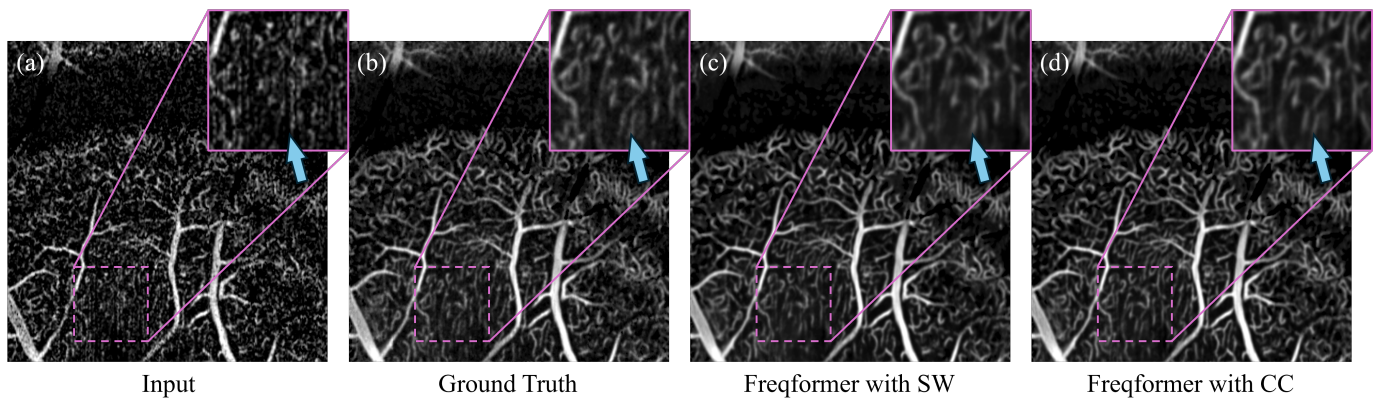


Fig. 5. Comparisons between Freqformer with cross-covariance (CC) attention and that with shifted window (SW) attention. Noted Freqformer with SW attention generates more blurred images and fails to reconstruct certain capillaries (indicated by blue arrow) when compared to those generated by Freqformer with CC attention.

connections, which hampers their ability to accurately reconstruct the complex capillary network. In contrast, transformer-based models, with their ability to capture long-range dependencies, generally reconstructed capillaries more effectively. Among all the tested methods, Freqformer achieved the most detailed reconstruction of capillaries with minimal blurring, outperforming both CNN-based and other transformer-based models. Notably, all methods successfully enhanced major blood vessels, as these structures are relatively simple and continuous.

The average image metrics across the test set are presented in Table I, with the best and second-best values highlighted in **bold** and underlined, respectively. Freqformer, achieved the best performance across all metrics. Compared to the second-best method (ART), Freqformer demonstrated a 0.32 dB improvement in PSNR and superior structural similarity, without increasing computational overhead in terms of giga multiply-accumulate operations per second (GMACs) or parameters (Params). While the CNN-based NAFNet performed competitively, even surpassing the transformer-based Restormer in certain metrics, its overall reconstruction capabilities remained inferior to the transformer models. As shown in Table I, transformer-based models generally outperform CNN-based models, though often requiring significantly higher GMACs and Params. Transformer-based models may have high space complexity, significantly increasing GPU memory usage. Among the transformer-based models, Freqformer required minimal GPU memory during training, half to that needed by Xformer or Restormer (Fig. 4). This efficient memory usage highlights Freqformer’s advantage in balancing performance and space efficiency.

D. Comparison with Shifted Window Mechanism

The common strategy for reducing space complexity is shifted window (SW) attention [41]. In order to reduce space complexity to a linear scale, SW attention operates by dividing the feature map into non-overlapping windows and applying conventional MHA within each window. To enable cross-window interaction, the windows are shifted by half their size. However, because the attention mechanism is applied locally

TABLE I
COMPARISON OF DIFFERENT MODELS IN ENHANCING RETINAL VASCULATURE.

Type	Methods	PSNR \uparrow	SSIM \uparrow	LPIPS \downarrow	GMACs (G)	Params (M)
CNN	DnCNN [36]	23.49	0.632	0.263	88.66	0.56
	RIDNet [37]	24.64	0.679	0.221	238.74	1.50
	SADNet [38]	25.22	0.697	0.212	43.08	4.23
	NAFNet [39]	26.09	0.723	0.205	38.98	29.16
Transformer	Restormer [33]	25.54	0.706	0.205	250.00	19.94
	Xformer [40]	26.44	0.740	0.198	325.26	25.15
	ART [34]	<u>26.58</u>	<u>0.743</u>	0.197	243.40	19.62
	Freqformer	26.90	0.754	0.193	248.70	19.97

within each window, SW attention may not fully capture long-range pixel interactions, even with window shifting. Consequently, SW attention may not fully leverage the power of the transformer architecture for global context representation.

Here, we replaced the cross-covariance (CC) attention in Freqformer with SW attention (window size 10×10). As shown in Figs. 5 (c) and (d), the capillaries generated by Freqformer with SW attention appeared more blurred compared to those generated by Freqformer with CC attention. Additionally, Freqformer with SW attention failed to reconstruct certain capillaries, as indicated by the blue arrow in the figure. In contrast, Freqformer with CC attention achieved superior image metrics while requiring relatively lower peak GPU memory, as summarized in Table II. This demonstrates that CC attention achieves high performance in reconstruction while requiring less space complexity, making it a more effective choice for high-resolution retinal OCTA reconstruction.

TABLE II
COMPARISON BETWEEN CROSS-COVARIANCE ATTENTION AND SHIFTED WINDOW ATTENTION

Methods	PSNR \uparrow	SSIM \uparrow	LPIPS \downarrow	Peak GPU Memory Usage (G)
Freqformer w/ CC	26.90	0.754	0.193	9.59
Freqformer w/ SW	26.64	0.743	0.198	11.38

E. Ablation Study

To validate the contributions of each component in Freqformer, we conducted ablation experiments on the proposed Transformer layer and the CFDM. The quantitative results are summarized in Table III.

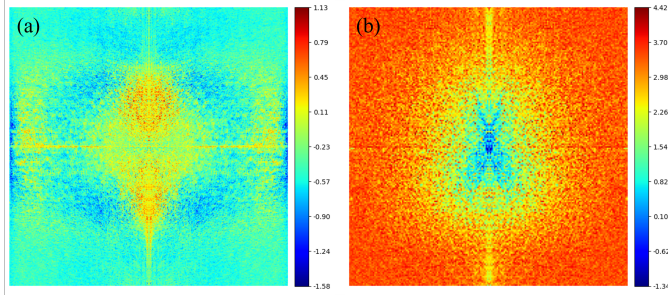


Fig. 6. Difference map calculated from the log-magnitude spectrum of the feature maps before and after the CFDM operation. (a) Difference map for the second CFDM in the first stage highlights the mild enhancement in low- and high- frequency components. (b) Difference map for the second CFDM in the second stage highlights the strong enhancement in mid- and high- frequency components.

•**Ablation for Sim-MHA and DFFN.** To establish a baseline, we replaced all Freqformer blocks with Residual Blocks (ResBlock). As shown in Table III, integrating the proposed Transformer layer (Sim-MHA and DFFN) into the model resulted in improved reconstruction performance across all the metrics. This demonstrates the importance of the Transformer’s global interaction capability, which significantly enhances feature extraction and reconstruction quality.

•**Ablation for CFDM.** We compared the performance of Freqformer with and without CFDM. The inclusion of CFDM yielded a notable 0.71 dB improvement in PSNR, underscoring its importance in achieving high-quality reconstruction. Notably, the CFDM contributed more to the improvements in LPIPS than the Transformer layer, highlighting its role in directly manipulating and enhancing all frequency components. While the Transformer primarily acts as a low-pass filter, CFDM complements it by refining both low- and high-frequency features, leading to a more balanced and comprehensive feature representation.

We further analyzed the functionality of CFDM by visualizing difference maps based on the log-magnitude spectrum of the feature maps before and after CFDM processing (Fig. 6). Our findings confirm that CFDM enhances specific frequency components selectively, depending on its location within the network. For instance, in Fig. 6 (a), CFDM moderately enhances low- and high- frequency components, whereas in Fig. 6 (b), CFDM strongly emphasizes mid- and high- frequency components. This targeted enhancement of frequency components demonstrates the effectiveness of CFDM in the frequency domain, providing superior visual performance compared to conventional pixel-wise enhancement in the spatial domain. The CFDM’s ability to adaptively focus on critical frequency ranges makes it a key contributor to the overall performance of Freqformer.

TABLE III
RESULTS OF ABLATION STUDY ON FREQFORMER COMPONENTS

ResBlock	Sim-MHA	DFFN	CFDM	PSNR \uparrow	SSIM \uparrow	LPIPS \downarrow
✓				25.88	0.717	0.206
	✓	✓		26.19	0.728	0.203
	✓	✓	✓	26.90	0.754	0.193

F. 3-D Visualization and Quantification of Retinal Circulation

The enhanced OCTA volume generated by Freqformer from single scan enabled detailed 3-D visualization of retinal circulation (Fig. 7). Notably, arteries and veins demonstrated unique perfusion networks. Avascular zones were clearly identified adjacent to arteries (indicated by white arrows), but were absent around veins (Fig. 7 (a)). Capillary vortices, which are a spider-like arrangement of capillaries in the deep capillary plexus (DCP), were resolved and confidently traced to their connection with retinal venules (Fig. 7 (b)). To quantify the retinal microvasculature in 3-D, we extracted capillary segments based on bifurcation point detection [32]. Specifically, we counted the capillary segment number, calculated the segment density within inner retinal volume, and analyzed the distribution of segment length. Both the enhanced OCTA volumes and merged OCTA volumes had more capillary segments (δ (M-S)/M: 20%, and δ (E-S)/M: 22%) than the original single scan volume (Fig. 7 (c)). Enhanced OCTA volumes demonstrated a higher frequency of longer capillary segments, validating the improved continuity of the vascular network. Statistical analysis showed no significant difference between the enhanced and merged volumes in capillary segment count ($p = 0.906$) or segment density ($p = 0.411$), suggesting that Freqformer effectively reconstructs the retinal vasculature to a level comparable with merged volumes. These findings demonstrate Freqformer’s capability to reconstruct discontinuous vascular fragments observed in single scan OCTA volumes, providing a robust tool for 3-D visualization and quantification of retinal microcirculation.

IV. DISCUSSION

A. Generalization Capability

To further assess the performance of Freqformer, we evaluated its generalization capability on OCTA images acquired using the same device and scan pattern but with larger fields of view (6×6 mm² and 12×12 mm²). These scan protocols are increasingly used in the clinical settings to capture larger pathological areas compared to the standard 3×3 mm² scans. However, with same A-line scanning rate and same (or slightly increased) A-line number, expanding the field of view results in lower scan density. This reduced density diminishes the quality of retinal microvasculature imaging, which cannot be fully compensated even by merging multiple volumes. Despite being pre-trained exclusively on 3×3 mm² scans, Freqformer successfully enhanced the image quality in images with larger fields of view (Fig. 8). These enhancements were evident in the improved connectivity of retinal major vessels and capillaries across all plexuses (NFLP, SCP, ICP, and DCP) as visualized in single depth plane images. The exceptional generalization performance of Freqformer demonstrates its potential to achieve super-resolution imaging for large-field-of-view scans without requiring high-definition ground truth from high-density scans—a significant advantage given the constraints of limited scanning rates in clinical devices. This capability highlights Freqformer’s robustness and versatility for broader clinical applications.

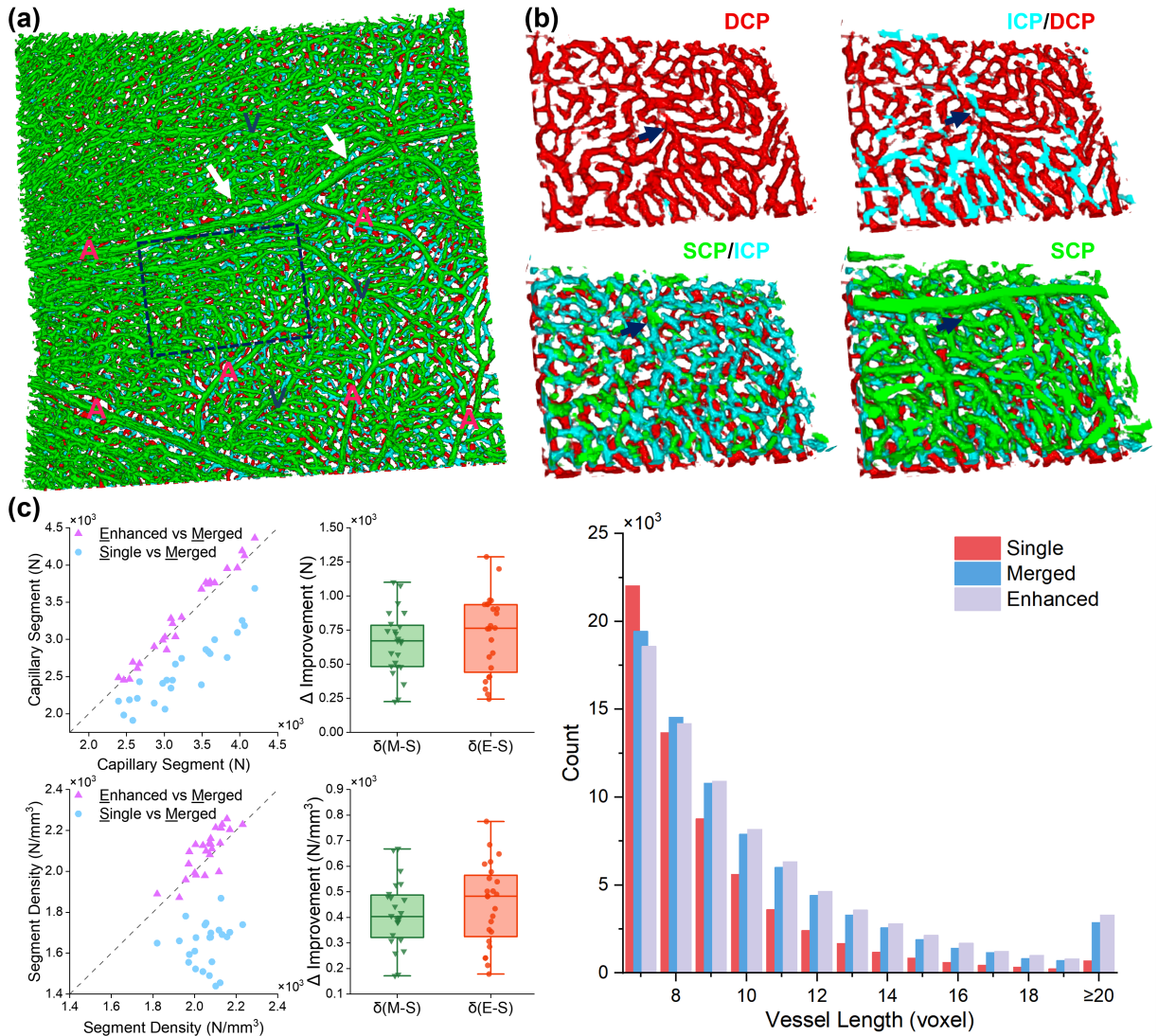


Fig. 7. 3-D visualization and quantification of retinal circulation. (a) Retinal circulation from enhanced OCTA volume, with SCP, ICP, DCP and inter-plexus capillaries color-coded in green, cyan, red, and combination of adjacent colors respectively. Avascular zones (arrows) were observed near arteries (A), but not in veins (V). (b) Zoomed-in view of 3-D retinal circulation at multiple depth, highlighting a vortex in DCP and its connection to veins in SCP. (c) Capillary segment count, density, and length histogram calculated in 3-D, as well as the comparisons between single scan, merged scan, and enhanced scan OCTA volumes ($N=24$).

B. Advantages of Enhanced 3-D OCTA Volume

Traditionally, OCTA scans are analyzed using projected 2-D *en face* images over a specified slab (depth range). These *en face* images offer higher SNR than single depth plane images, making them well-suited for visualizing retinal microvasculature and training deep learning models for enhancement [10], [12]. Unfortunately, the depth information is collapsed in these 2-D images, thereby hindering the appreciation and quantification of 3-D retinal microvasculature network. Although some studies have explored 3-D visualization of OCTA, they have primarily focused on segmenting binary masks of blood vessels [42]. This approach neglects the de-correlation angiogram information inherent to OCTA volume, which is closely linked to blood flow rate [15] and serves as a robust biomarker for retinal diseases such as diabetic retinopathy (DR) [43].

In contrast, the enhanced high-definition OCTA volumes generated by Freqformer preserve flow information for comprehensive volumetric analysis of the retinal microvasculature. Here with Freqformer, we revealed the organization of retinal arteries and veins and extract the capillary segments in 3-D (Fig. 7). Using this data provided with commercial OCT, we successfully quantified the capillary segment density *in vivo* in 3-D for human retinas for the first time. In the future, we hope that more detailed quantification of 3-D microvasculature would provide us more insight into the blood flow and retinal tissue oxygenation [44].

C. Limitations

While the results demonstrate substantial improvements of Freqformer in both visual and quantitative performance

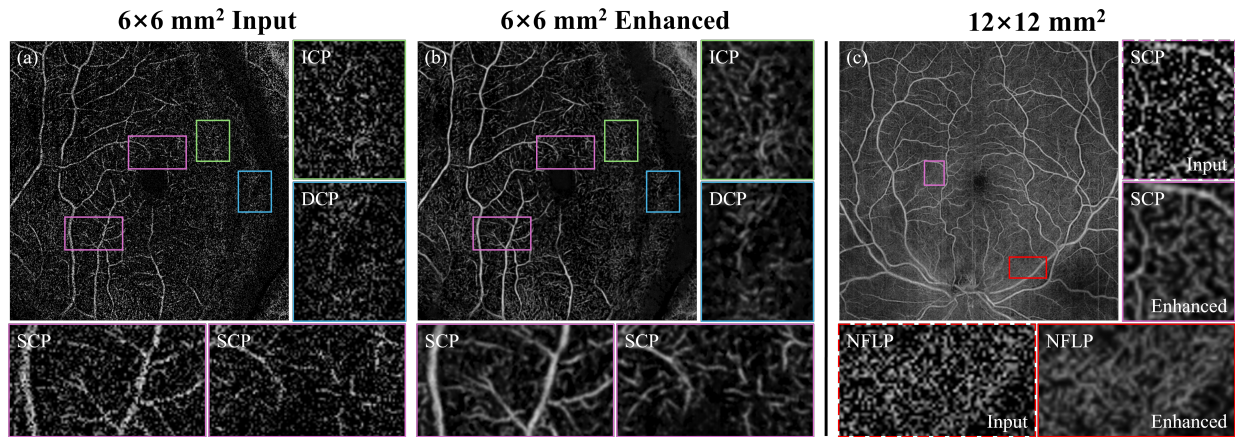


Fig. 8. Generalization results of Freqformer (trained with 3×3 mm² scans) on 6×6 mm² and 12×12 mm² scans. (a) and (b) display the depth plane image of the single scan and the enhanced image, respectively. (c) displays the enhanced 2-D projection image from internal limiting membrane (ILM) to outer plexiform layer (OPL).

compared to other methods, there are several limitations that may affect its broader applicability and impact. First, Freqformer’s reliance on high-definition ground truth derived from merged OCTA volumes presents a limitation, particularly in clinical settings where multiple scans may not be feasible due to patient comfort, time constraints, or technical limitations. This dependency on merged volumes means that Freqformer may not perform optimally on single-scan data without high-definition references, limiting its utility in certain real-world applications. Second, despite our efforts to optimize space complexity, the computational demand of transformer network may limit the deployment of Freqformer in clinical environments lacking high-performance GPU hardware. Further research into streamlining the architecture or adapting it for less powerful devices would improve Freqformer’s accessibility and ease of use. Third, our study involved only healthy subjects. Although we anticipate Freqformer can be applied directly or with minimal customization to pathological cases, the unique vascular patterns—such as capillary dropout or increased vessel tortuosity in diseased retinas—may challenge its generalizability across diverse patient populations, especially in scans with a large field of view. Future studies to evaluate and potentially adapt Freqformer for such pathologic cases will be necessary to confirm its broader applicability.

V. CONCLUSION

In conclusion, this study presents Freqformer, a novel frequency-domain Transformer architecture designed to enhance 3-D visualization of retinal circulation in OCTA images. By integrating a cross-covariance attention mechanism and a complex-valued frequency-domain module, Freqformer effectively addresses limitations of conventional OCTA processing, delivering detailed, high-definition visualizations of retinal microvasculature with improved capillary continuity and reduced noise. Experimental results demonstrate that Freqformer outperforms state-of-the-art CNN-based and Transformer-based methods, offering superior enhancement and generalizability across different fields of view. The enhanced 3-D OCTA

volumes enable an in-depth analysis of retinal vascular structures, revealing critical features such as capillary vortices and avascular zones, which are essential for understanding retinal health and disease. Despite limitations, including computational demand and reliance on high-definition ground truth during training, Freqformer shows significant promise as a powerful tool for retinal imaging. Future efforts will focus on optimizing Freqformer for clinical deployment, enhancing its efficiency, and expanding its capabilities for flow quantification and the analysis of diseased retinas. These advancements will further solidify Freqformer’s role in advancing the diagnosis and monitoring of retinal vascular diseases.

REFERENCES

- [1] T. R. Taylor, M. J. Menten, D. Rueckert, S. Sivaprasad, and A. J. Lotery, “The role of the retinal vasculature in age-related macular degeneration: a spotlight on octa,” *Eye*, vol. 38, no. 3, pp. 442–449, 2024.
- [2] Y. Jia, O. Tan, J. Tokayer, B. Potsaid, Y. Wang, J. J. Liu, M. F. Kraus, H. Subhash, J. G. Fujimoto, J. Hornegger *et al.*, “Split-spectrum amplitude-decorrelation angiography with optical coherence tomography,” *Optics express*, vol. 20, no. 4, pp. 4710–4725, 2012.
- [3] G. Chan, C. Balaratnasingam, J. Xu, Z. Mammo, S. Han, P. Mackenzie, A. Merkur, A. Kirker, D. Albani, M. V. Sarunic *et al.*, “In vivo optical imaging of human retinal capillary networks using speckle variance optical coherence tomography with quantitative clinico-histological correlation,” *Microvascular research*, vol. 100, pp. 32–39, 2015.
- [4] A. Ishibazawa, L. R. De Pretto, A. Y. Alibhai, E. M. Moul, M. Arya, O. Sorour, N. Mehta, C. R. Baumal, A. J. Witkin, A. Yoshida *et al.*, “Retinal nonperfusion relationship to arteries or veins observed on wide-field optical coherence tomography angiography in diabetic retinopathy,” *Investigative Ophthalmology & Visual Science*, vol. 60, no. 13, pp. 4310–4318, 2019.
- [5] R. K. Meleppat, E. B. Miller, S. K. Manna, P. Zhang, E. N. Pugh Jr, and R. J. Zawadzki, “Multiscale hessian filtering for enhancement of oct angiography images,” in *Ophthalmic technologies XXIX*, vol. 10858. SPIE, 2019, pp. 64–70.
- [6] P. T. Truc, M. A. Khan, Y.-K. Lee, S. Lee, and T.-S. Kim, “Vessel enhancement filter using directional filter bank,” *Computer Vision and Image Understanding*, vol. 113, no. 1, pp. 101–112, 2009.
- [7] H. Liu, S. Lin, C. Ye, D. Yu, J. Qin, and L. An, “Using a dual-tree complex wavelet transform for denoising an optical coherence tomography angiography blood vessel image,” *OSA Continuum*, vol. 3, no. 9, pp. 2630–2645, 2020.
- [8] L. Wang, Z. Chen, Z. Zhu, X. Yu, and J. Mo, “Compressive-sensing swept-source optical coherence tomography angiography with reduced noise,” *Journal of Biophotonics*, vol. 15, no. 8, p. e202200087, 2022.

- [9] X. Tan, X. Chen, Q. Meng, F. Shi, D. Xiang, Z. Chen, L. Pan, and W. Zhu, "Oct2former: A retinal oct-angiography vessel segmentation transformer," *Computer Methods and Programs in Biomedicine*, vol. 233, p. 107454, 2023.
- [10] M. Gao, Y. Guo, T. T. Hormel, J. Sun, T. S. Hwang, and Y. Jia, "Reconstruction of high-resolution 6×6 -mm oct angiograms using deep learning," *Biomedical Optics Express*, vol. 11, no. 7, pp. 3585–3600, 2020.
- [11] X. Yuan, Y. Huang, L. An, J. Qin, G. Lan, H. Qiu, B. Yu, H. Jia, S. Ren, H. Tan *et al.*, "Image enhancement of wide-field retinal optical coherence tomography angiography by super-resolution angiogram reconstruction generative adversarial network," *Biomedical Signal Processing and Control*, vol. 78, p. 103957, 2022.
- [12] S. Kadomoto, A. Uji, Y. Muraoka, T. Akagi, and A. Tsujikawa, "Enhanced visualization of retinal microvasculature in optical coherence tomography angiography imaging via deep learning," *Journal of Clinical Medicine*, vol. 9, no. 5, p. 1322, 2020.
- [13] S. Stefan and J. Lee, "Deep learning toolbox for automated enhancement, segmentation, and graphing of cortical optical coherence tomography microangiograms," *Biomedical Optics Express*, vol. 11, no. 12, pp. 7325–7342, 2020.
- [14] M. Li, K. Huang, C. Zeng, Q. Chen, and W. Zhang, "Visualization and quantization of 3d retinal vessels in octa images," *Optics Express*, vol. 32, no. 1, pp. 471–481, 2024.
- [15] J. P. Su, R. Chandwani, S. S. Gao, A. D. Pechauer, M. Zhang, J. Wang, Y. Jia, D. Huang, and G. Liu, "Calibration of optical coherence tomography angiography with a microfluidic chip," *Journal of biomedical optics*, vol. 21, no. 8, pp. 086015–086015, 2016.
- [16] A. Vaswani, N. Shazeer, N. Parmar, J. Uszkoreit, L. Jones, A. N. Gomez, Ł. Kaiser, and I. Polosukhin, "Attention is all you need," *Advances in neural information processing systems*, vol. 30, 2017.
- [17] B. Yao, L. Jin, J. Hu, Y. Liu, Y. Yan, Q. Li, and Y. Lu, "Pscat: a lightweight transformer for simultaneous denoising and super-resolution of oct images," *Biomedical Optics Express*, vol. 15, no. 5, pp. 2958–2976, 2024.
- [18] X. Li, H. Liu, X. Song, C. C. Marboe, B. C. Brott, S. H. Litovsky, and Y. Gan, "Structurally constrained and pathology-aware convolutional transformer generative adversarial network for virtual histology staining of human coronary optical coherence tomography images," *Journal of Biomedical Optics*, vol. 29, no. 3, pp. 036004–036004, 2024.
- [19] B. Wang, R. Brown, J. Chhablani, and S. Pi, "Volumetrically tracking retinal and choroidal structural changes in central serous chorioretinopathy," *Biomedical Optics Express*, vol. 14, no. 10, pp. 5528–5538, 2023.
- [20] S. Pi, T. T. Hormel, X. Wei, W. Cepurna, J. C. Morrison, and Y. Jia, "Imaging retinal structures at cellular-level resolution by visible-light optical coherence tomography," *Optics letters*, vol. 45, no. 7, pp. 2107–2110, 2020.
- [21] M. T. Bernucci, C. W. Merkle, and V. J. Srinivasan, "Investigation of artifacts in retinal and choroidal oct angiography with a contrast agent," *Biomedical optics express*, vol. 9, no. 3, pp. 1020–1040, 2018.
- [22] M. Zhang, T. S. Hwang, J. P. Campbell, S. T. Bailey, D. J. Wilson, D. Huang, and Y. Jia, "Projection-resolved optical coherence tomographic angiography," *Biomedical optics express*, vol. 7, no. 3, pp. 816–828, 2016.
- [23] Y. Liu, A. Carass, A. Filippatou, Y. He, S. D. Solomon, S. Saidha, P. A. Calabresi, and J. L. Prince, "Projection artifact suppression for inner retina in oct angiography," in *2019 IEEE 16th International Symposium on Biomedical Imaging (ISBI 2019)*. IEEE, 2019, pp. 592–596.
- [24] Y. Li and J. Tang, "Blood vessel tail artifacts suppression in optical coherence tomography angiography," *Neurophotonics*, vol. 9, no. 2, pp. 021906–021906, 2022.
- [25] A. Ali, H. Touvron, M. Caron, P. Bojanowski, M. Douze, A. Joulin, I. Laptev, N. Neverova, G. Synnaeve, J. Verbeek *et al.*, "Xcit: Cross-covariance image transformers," *Advances in neural information processing systems*, vol. 34, pp. 20014–20027, 2021.
- [26] A. Trockman and J. Z. Kolter, "Mimetic initialization of self-attention layers," in *International Conference on Machine Learning*. PMLR, 2023, pp. 34456–34468.
- [27] B. He and T. Hofmann, "Simplifying transformer blocks," *arXiv preprint arXiv:2311.01906*, 2023.
- [28] N. Park and S. Kim, "How do vision transformers work?" *arXiv preprint arXiv:2202.06709*, 2022.
- [29] X. Li, Z. Dong, H. Liu, J. J. Kang-Mieler, Y. Ling, and Y. Gan, "Frequency-aware optical coherence tomography image super-resolution via conditional generative adversarial neural network," *Biomedical Optics Express*, vol. 14, no. 10, pp. 5148–5161, 2023.
- [30] L. Wang, S. Chen, L. Liu, X. Yin, G. Shi, and J. Mo, "Axial super-resolution optical coherence tomography via complex-valued network," *Physics in Medicine & Biology*, vol. 68, no. 23, p. 235016, 2023.
- [31] C. Trabelsi, O. Bilaniuk, Y. Zhang, D. Serdyuk, S. Subramanian, J. F. Santos, S. Mehri, N. Rostamzadeh, Y. Bengio, and C. J. Pal, "Deep complex networks," *arXiv preprint arXiv:1705.09792*, 2017.
- [32] S. Pi, T. T. Hormel, X. Wei, W. Cepurna, B. Wang, J. C. Morrison, and Y. Jia, "Retinal capillary oximetry with visible light optical coherence tomography," *Proceedings of the National Academy of Sciences*, vol. 117, no. 21, pp. 11658–11666, 2020.
- [33] S. W. Zamir, A. Arora, S. Khan, M. Hayat, F. S. Khan, and M.-H. Yang, "Restormer: Efficient transformer for high-resolution image restoration," in *Proceedings of the IEEE/CVF conference on computer vision and pattern recognition*, 2022, pp. 5728–5739.
- [34] J. Zhang, Y. Zhang, J. Gu, Y. Zhang, L. Kong, and X. Yuan, "Accurate image restoration with attention retractable transformer," in *ICLR*, 2023.
- [35] I. Loshchilov and F. Hutter, "Decoupled weight decay regularization," in *International Conference on Learning Representations*, 2019. [Online]. Available: <https://openreview.net/forum?id=Bkg6RiCqY7>
- [36] K. Zhang, W. Zuo, Y. Chen, D. Meng, and L. Zhang, "Beyond a gaussian denoiser: Residual learning of deep cnn for image denoising," *IEEE transactions on image processing*, vol. 26, no. 7, pp. 3142–3155, 2017.
- [37] S. Anwar and N. Barnes, "Real image denoising with feature attention," in *Proceedings of the IEEE/CVF international conference on computer vision*, 2019, pp. 3155–3164.
- [38] M. Chang, Q. Li, H. Feng, and Z. Xu, "Spatial-adaptive network for single image denoising," in *Computer Vision—ECCV 2020: 16th European Conference, Glasgow, UK, August 23–28, 2020, Proceedings, Part XXX 16*. Springer, 2020, pp. 171–187.
- [39] L. Chen, X. Chu, X. Zhang, and J. Sun, "Simple baselines for image restoration," in *European conference on computer vision*. Springer, 2022, pp. 17–33.
- [40] J. Zhang, Y. Zhang, J. Gu, J. Dong, L. Kong, and X. Yang, "Xformer: Hybrid x-shaped transformer for image denoising," *arXiv preprint arXiv:2303.06440*, 2023.
- [41] Z. Liu, Y. Lin, Y. Cao, H. Hu, Y. Wei, Z. Zhang, S. Lin, and B. Guo, "Swin transformer: Hierarchical vision transformer using shifted windows," in *Proceedings of the IEEE/CVF international conference on computer vision*, 2021, pp. 10012–10022.
- [42] D. M. Sampson, A. M. Dubis, F. K. Chen, R. J. Zawadzki, and D. D. Sampson, "Towards standardizing retinal optical coherence tomography angiography: a review," *Light: science & applications*, vol. 11, no. 1, p. 63, 2022.
- [43] A. K. Dadzie, D. Le, M. Abtahi, B. Ebrahimi, T. Son, J. I. Lim, and X. Yao, "Normalized blood flow index in optical coherence tomography angiography provides a sensitive biomarker of early diabetic retinopathy," *Translational Vision Science & Technology*, vol. 12, no. 4, pp. 3–3, 2023.
- [44] B. A. Corliss, C. Mathews, R. Doty, G. Rohde, and S. M. Peirce, "Methods to label, image, and analyze the complex structural architectures of microvascular networks," *Microcirculation*, vol. 26, no. 5, p. e12520, 2019.